# Coupling of lattice, spin, and intraconfigurational excitations of $Eu^{3+}$ in $Eu_2ZnIrO_6$

Birender Singh,[1,*] M. Vogl,[2] S. Wurmehl,[2,3] S. Aswartham,[2] B. Büchner,[2,3] and Pradeep Kumar[1,†]

[1]*School of Basic Sciences, Indian Institute of Technology Mandi, Mandi-175005, India*

[2]*Leibniz-Institute for Solid-State and Materials Research, IFW-Dresden, 01069 Dresden, Germany*

[3]*Institute of Solid-State Physics, TU Dresden, 01069 Dresden, Germany*

(Received 9 June 2020; revised 18 August 2020; accepted 13 October 2020; published 3 November 2020)

In $Eu_2ZnIrO_6$, effectively two atoms are active; i.e., Ir is magnetically active, which results in complex magnetic ordering within the Ir sublattice at low temperature. On the other hand, although Eu is a Van Vleck paramagnet, it is active in the electronic channels involving $4f^6$ crystal-field split levels. Phonons, quanta of lattice vibration involving vibration of atoms in the unit cell, are intimately coupled with both magnetic and electronic degrees of freedom (DOF). Here, we report a comprehensive study focusing on the phonons as well as intraconfigurational excitations in double-perovskite $Eu_2ZnIrO_6$. Our studies reveal strong coupling of phonons with the underlying magnetic DOF reflected in the renormalization of the phonon self-energy parameters well above the spin-solid phase ($T_N \sim 12$ K) until temperature as high as $\sim 3T_N$ evidences broken spin rotational symmetry deep into the paramagnetic phase. In particular, all the observed first-order phonon modes show softening of varying degree below $\sim 3T_N$, and low-frequency phonons become sharper, while the high-frequency phonons show broadening attributed to the additional available magnetic damping channels. We also observed a large number of high-energy modes, 39 in total, attributed to the electronic transitions between $4f$ levels of the rare-earth $Eu^{3+}$ ion and these modes shows anomalous temperature evolution as well as mixing of the crystal-field split levels attributed to the strong coupling of electronic and lattice DOF.

DOI: 10.1103/PhysRevResearch.2.043179

## I. INTRODUCTION

A tremendous interest in iridates has been seen in the past few years due to a realization of the exotic quantum phases of matter ascribed to the strong spin-orbit coupling (SOC), electronic correlations, and their entanglement [1–12]. Double-perovskite iridium oxides of $A_2BIrO_6$ structure are of particular interest because of the complex quantum magnetic ground states in these materials. Their magnetic ground state is quite enigmatic; it strongly depends on the choice of $A$- and $B$-site elements, that also provide an opportunity to tune the nature of magnetic interactions. It is anticipated that such tuning of these interactions may also give rise to the much sought after quantum spin-liquid state in these double perovskites considered to be the holy grail of condensed matter physics. Despite advances in understanding of different magnetic interactions, such as Heisenberg and Kitaev type, in these systems with the substitution of $3d$ transition metal elements (magnetic and nonmagnetic) of varying ionic radii at the $B$ site, i.e., $A_2YIrO_6$ ($A$ = Ba, Sr) and $La_2BIrO_6$ ($B$ = Cu, Zn) [13–20], these iridates continue to surprise us. Where the $A$ site is occupied by an alkaline and/or rare-earth La element, detailed investigations of the complex magnetic behavior with other rare-earth elements at the $A$ site are not much explored, such as $Ln_2CoIrO_6$ ($Ln$ = Eu, Tb, and Ho) and $Ln_2ZnIrO_6$ ($Ln$ = Sm, Nd) [21–23].

$Eu_2ZnIrO_6$ adopts a monoclinic double-perovskite structure with the space group $P2_1/n$ (no. 14) [24]. $Eu^{3+}$ ($4f^6$, $S = 3$, $L = 3$) is at the eightfold coordinated $A$ site, whereas the $B$ site is occupied by $Zn^{2+}$ ($3d^{10}$; spin $S = 0$), and the $Ir^{4+}$ state with $5d^5$ in pseudospin $J_{\text{eff}} = \frac{1}{2}$ occupies two different crystallographic sites in the corner-sharing octahedral environment. $Eu_2ZnIrO_6$ shows a ferromagnetic and/or canted antiferromagneticlike transition at $T_N \sim 12$ K attributed to the ordering of spin associated with the Ir sublattice as $Ir^{4+}$ is the only magnetic ion in this compound, and $Eu^{3+}$ is a Van Vleck paramagnetic ion [24,25]. In $Eu_2ZnIrO_6$, the $Eu^{3+}$ ion occupies the $C_1$ low-symmetry site, and therefore provides an opportunity to probe electronic degrees of freedom via potential electronic transitions between the different $4f$-level multiplets. In these systems magnetic, electronic, and lattice degrees of freedom attract a great deal of attention as they are believed to be the main controlling factors central to their underlying physics. A very important aim in the study of Ir based double perovskites is to elucidate their ground states and the contribution of different DOF. Here, we have undertaken such a study focusing on the intricate coupling between these three DOF, i.e., lattice, magnetic, and electronic. We have used inelastic light (Raman) scattering as a tool to understand the coupling between these quasiparticle excitations.

*birender.physics5390@gmail.com

†pkumar@iitmandi.ac.in

Raman spectroscopy is a sensitive and effective technique for probing the underlying lattice, magnetic, and electronic degrees of freedom, and is extensively used to unravel the coupling between a range of quasiparticles in solids such as magnons, orbitons, excitons, and phonons [23,26–34]. It is basically a photon-in photon-out process in which an incident photon of energy $\omega_i$ is inelastically scattered by the system under consideration into a photon of energy $\omega_s$. For a Stokes process, quasiparticle excitations with energy $\Delta\omega(\text{Raman shift}) = \omega_i - \omega_s$ are created in the solid. Hence, Raman scattering can be employed to investigate the crucial role of coupling between lattice and electronic degrees of freedom, involving crystal-field excitations of rare-earth elements, to the modulation of magnetic and thermodynamical properties associated with double-perovskite iridates. Within this scenario, the crystal-field structure of $4f$ levels of rare-earth elements allows further understanding of the fascinating ground-state properties associated with these double-perovskite materials. In this paper, we report systematic and detailed lattice-dynamics studies and intraconfigurational excitations, involving crystal-field split multiplets of the $Eu^{3+}$ ion for $Eu_2ZnIrO_6$ using inelastic light (Raman) scattering as a function of temperature along with the density functional theory based calculations to understand the complex interactions among spin, lattice, and electronic DOF. We observe a pronounced coupling of lattice with spin excitations and intraconfigurational electronic transition modes of $Eu^{3+}$ ions, reflected via anomalous temperature dependence of the self-energy parameters (i.e., phonon frequency and linewidth). Phonon modes started showing softening at a temperature as high as $\sim 3T_N$, clearly suggesting an existence of short-range magnetic correlation deep inside the paramagnetic phase. The Brillouin zone centered calculated eigenvectors show that low-frequency phonon modes are mainly due to the vibration of Eu atoms, while the high-frequency modes correspond to the displacement of oxygen atoms associated with the $Zn/IrO_6$ octahedra. Our observation of two sharp and intense electronic transition modes from the nondegenerate singlet excited state ($^5D_0$) to the singlet ground state ($^7F_0$) evidence the presence of two nonequivalent $Eu^{3+}$ sites within the crystal structure. Furthermore, the assignment of symmetry of different phonon modes is done in accordance to our density functional theory based calculations.

## II. EXPERIMENTAL AND COMPUTATIONAL DETAILS

The synthesis process and detailed characterization of these high-quality polycrystalline $Eu_2ZnIrO_6$ samples are described in detail in Ref. [24]. Inelastic light (Raman) scattering measurements were performed via Raman spectrometer (LabRAM HR Evolution) in quasibackscattering configuration using a linearly polarized laser of 532 nm (2.33 eV) and 633 nm (1.96 eV) wavelength (energy) at low power, less than $\sim$1 mW, to avoid local heating effects. A 50× long working distance objective was used to focus the laser on the sample surface and the spectra were dispersed through a grating with a density of 600 lines/mm. A Peltier cooled charged-coupled device detector was employed to collect the dispersed light. Temperature variation was done from 4 to 330 K using a continuous He-flow closed-cycle cryostat (Montana Instruments) with a temperature accuracy of $\pm 0.1$ K or even better temperature accuracy.

The calculations of zone-centered phonons were done using the plane-wave approach implemented in QUANTUM ESPRESSO [35]. All the calculations were carried out using generalized gradient approximation with Perdew-Burke-Ernzerhof as an exchange-correlation function. The plane-wave cutoff energy and charge density cutoff were set to 60 and 280 Ry, respectively. Dynamical matrix and eigenvectors were determined using density functional perturbation theory [36]. The numerical integration over the Brillouin zone was done with a $4 \times 4 \times 4$ $k$-point sampling mesh in the Monkhorst-Pack grid [37]. In our calculations, we used fully relaxed ionic positions with experimental lattice parameters given in Ref. [24].

## III. RESULTS AND DISCUSSION

### A. Raman-scattering and lattice-dynamics calculations

$Eu_2ZnIrO_6$ crystals have double-perovskite monoclinic structure belonging to space group $P2_1/n$ (No. 14) [24]. The factor-group analysis predicts a total of 60 modes in the irreducible representation, out of which 24 are Raman active and 36 correspond to infrared active modes (see Table I for details). Figure 1(a) shows the Raman spectra in a wide spectral range of 40–5500 $\text{cm}^{-1}$ at 4 K. The spectrum is fitted with a sum of Lorentzian functions to extract frequency ($\omega$), linewidth ($\Gamma$) [full width at half maxima (FWHM)], and the integrated intensity along with the corresponding error bars of different modes [see Figs. 1(b) and 1(c)], where solid blue lines are the individual peak fits and the solid red line represents a total fit.

In order to decipher the symmetry and associated eigenvectors (atomic displacements) of different vibrational modes, we performed Brillouin zone centered $\Gamma = (0, 0, 0)$ lattice-dynamics calculations using density functional theory (DFT). We note that our calculated zone-centered phonon frequencies are in very good agreement with the experimentally observed frequencies of the modes below 750 $\text{cm}^{-1}$ at 4 K, labeled as S1–S17 [see Fig. 1(b) and Table II]. Based on our first-principle calculations, we have assigned these modes below $\sim$750 $\text{cm}^{-1}$, i.e., modes S1–S17, as the first-order phonon modes, while high-frequency modes in the frequency range of 1000–1400 $\text{cm}^{-1}$, i.e., S18–S20, have been assigned as second-order phonon modes. The difference between calculated and experimental phonon frequency value at 4 K is determined via absolute relative average difference formula $|\overline{\omega_r}|_{\%} = \frac{100}{N}\sum_i |\frac{\omega_i^{\text{calc}} - \omega_i^{\text{expt}}}{\omega_i^{\text{expt}}}|$, where $i = 1, 2, \ldots, N$ is the number of Raman active modes (17 here), and $|\overline{\omega_r}|_{\%}$ is $\sim$1.5% (obtained value). Furthermore, the symmetry assignment of different phonon modes is done in accordance to our first-principle lattice-dynamics calculations as shown in Table II. We notice from the visualization of phonon eigenvectors (see Fig. 2) that the low-frequency phonon modes S1–S5 arise due to the displacement of Eu atoms; however, the high-frequency phonon modes S6–S17 comprise the bending and stretching vibrations of Zn/Ir-O bonds associated with corner-sharing $Zn/IrO_6$ octahedra. Furthermore, we also calculated full phonon dispersion and phonon density of states

TABLE I. Wyckoff positions and irreducible representations of the phonon modes, at the gamma point of the Brillouin zone, of the monoclinic ($P2_1/n$; space group No. 14) double-perovskite $Eu_2ZnIrO_6$. $\Gamma_{total}$, $\Gamma_{Raman}$, and $\Gamma_{infrared}$ represent the total normal modes, the Raman, and the infrared active modes, respectively.

| $P2_1/n$; space group No. 14 | | |
|---|---|---|
| Atom | Wyckoff site | Mode decomposition |
| Eu | 4*e* | $3A_g + 3A_u + 3B_g + 3B_u$ |
| Zn | 2*d* | $3A_u + 3B_u$ |
| Ir | 2*c* | $3A_u + 3B_u$ |
| O(1) | 4*e* | $3A_g + 3A_u + 3B_g + 3B_u$ |
| O(2) | 4*e* | $3A_g + 3A_u + 3B_g + 3B_u$ |
| O(3) | 4*e* | $3A_g + 3A_u + 3B_g + 3B_u$ |
| | $\Gamma_{total} = 12A_g + 18A_u + 18B_u + 12B_g$ | |
| | $\Gamma_{Raman} = 12A_g + 12B_g$ and $\Gamma_{infrared} = 18A_u + 18B_u$ | |

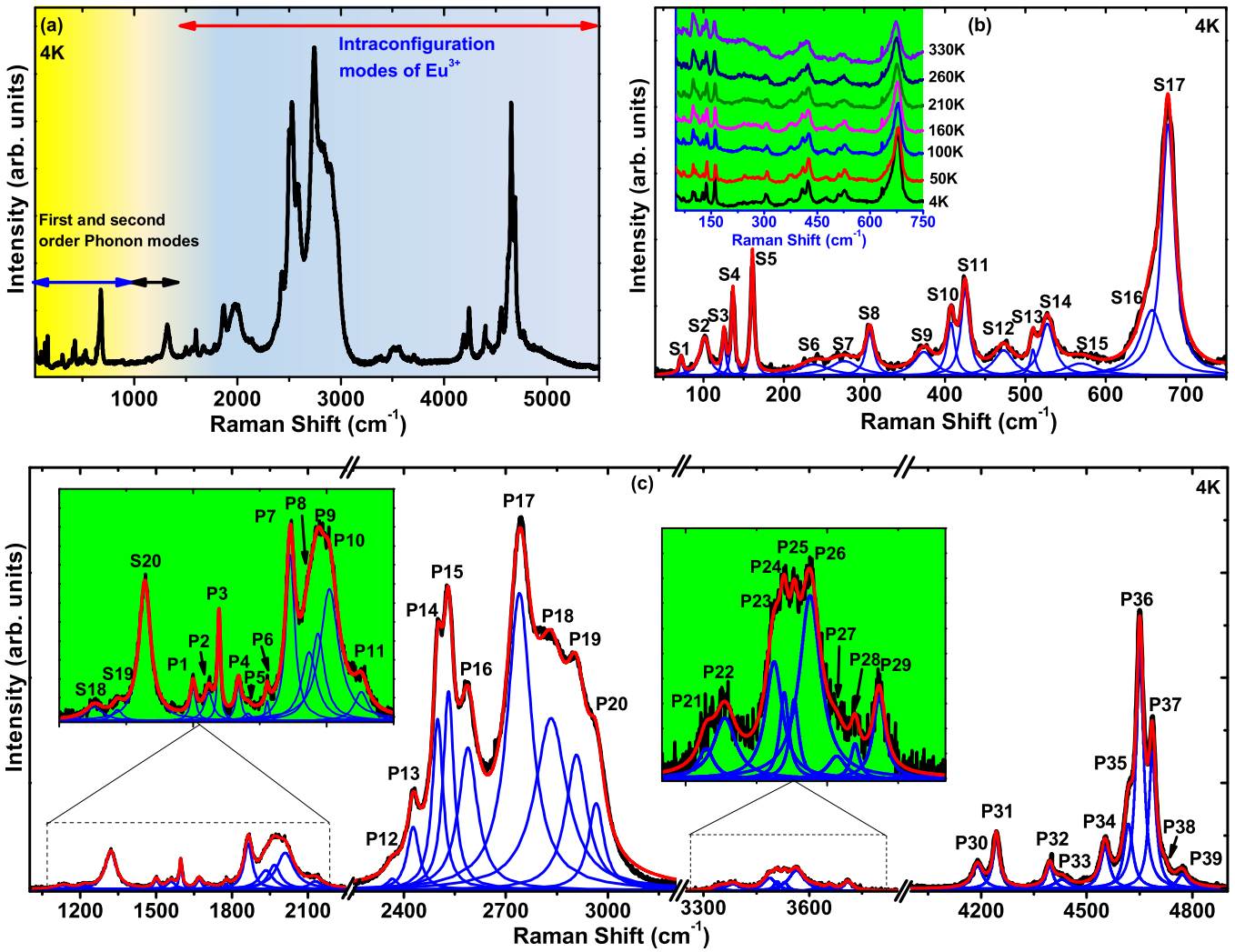


FIG. 1. (a) Raman spectra of $Eu_2ZnIrO_6$ recorded at 4 K in the spectral range of 40–5500 $cm^{-1}$ using 532-nm laser. Yellow, light yellow, and light blue shaded area indicates first-order and second-order phonon modes and intraconfigurational modes of $Eu^{3+}$ ions in $Eu_2ZnIrO_6$, respectively. (b) Raman spectra of first-order phonon modes in the spectral range of 40–750 $cm^{-1}$ fitted with a sum of Lorentzian functions, where the solid thick red line indicates a total fit to the experimental data and the solid thin blue line corresponds to individual peak fit; inset shows temperature evolution of the spectrum in the temperature range of 4–330 K. (c) High-energy Raman spectrum fitted with a sum of Lorentzian functions in the spectral range of 1000–4900 $cm^{-1}$. The inset shows the amplified spectrum in the frequency range of 1000–2250 $cm^{-1}$ and 3300–3800 $cm^{-1}$.

TABLE II. List of the experimentally observed Raman active phonon mode frequencies at 4 K (monoclinic space group $P2_1/n$) with 532-nm excitation laser along with the DFT based calculated zone centered frequencies. Fitting parameters obtained using equations as described in the text, and estimated values of spin-phonon coupling constant ($\lambda_{sp}$) for the prominent phonon modes. The symmetry assignment of phonon modes is done in accordance to our lattice-dynamics calculations. The low-frequency modes S1–S5 are mainly attributed to the vibrations of the Eu atoms, while high-frequency modes S6–S17 are associated with the bending and stretching of Zn/Ir-O bonds in the $Zn/IrO_6$ octahedral units. The calculated frequencies not observed experimentally are 93.5 ($B_g$), 207.4 ($B_g$), 208.1 ($A_g$), 293.0 ($A_g$), 356.2 ($A_g$), 411.7 ($B_g$), and 521.0 ($A_g$). Units are in $cm^{-1}$.

| | | | | Fitted parameters | | | | | |
|---|---|---|---|---|---|---|---|---|---|
| Mode assignment | Expt. $\omega$ (4 K) | DFT $\omega$ | $\lambda_{sp}$ | $\omega_0$ | $A$ | $B$ | $\Gamma_0$ | $C$ | $D$ |
| S1-$B_g$ (Eu) | 71.1 | 87.8 | | | | | | | |
| S2-$A_g$ (Eu) | 101.6 | 95.9 | 8.2 | 103.8 ± 0.2 | –0.19 ± 0.07 | –0.003 ± 0.002 | 9.2 ± 0.7 | 0.39 ± 0.03 | 0.005 ± 0.001 |
| S3-$A_g$ (Eu) | 125.6 | 119.8 | | 126.6 ± 0.2 | 0.08 ± 0.01 | –0.006 ± 0.002 | 5.1 ± 0.4 | –0.04 ± 0.02 | 0.003 ± 0.001 |
| S4-$A_g$ (Eu) | 136.6 | 125.7 | 5.9 | 137.6 ± 0.2 | 0.27 ± 0.12 | –0.016 ± 0.003 | 4.2 ± 0.3 | 0.21 ± 0.01 | 0.008 ± 0.004 |
| S5-$B_g$ (Eu) | 160.8 | 152.1 | 7.4 | 162.8 ± 0.2 | –0.18 ± 0.14 | –0.017 ± 0.005 | 4.3 ± 0.3 | 0.19 ± 0.02 | 0.011 ± 0.007 |
| S6-$A_g$ (O) | 237.4 | 237.9 | | 242.1 ± 1.2 | 5.32 ± 0.96 | –0.42 ± 0.05 | 20.9 ± 2.1 | 4.79 ± 1.08 | 0.187 ± 0.021 |
| S7-$B_g$ (O) | 273.7 | 284.3 | | 277.1 ± 2.6 | 5.42 ± 2.09 | –0.51 ± 0.11 | 17.4 ± 3.4 | 1.37 ± 0.49 | –0.173 ± 0.091 |
| S8-$B_g$ (O) | 306.5 | 302.1 | 7.3 | 308.3 ± 0.5 | 0.30 ± 0.11 | –0.18 ± 0.032 | 7.5 ± 1.8 | 1.72 ± 1.12 | 0.109 ± 0.015 |
| S9-$B_g$ (O) | 373.6 | 364.8 | | 375.5 ± 1.5 | 0.79 ± 1.41 | –0.37 ± 0.11 | 15.9 ± 3.3 | 1.19 ± 1.01 | 0.008 ± 0.003 |
| S10-$A_g$ (O) | 407.6 | 408.0 | 6.3 | 409.1 ± 1.1 | –0.27 ± 0.11 | –0.24 ± 0.10 | 10.1 ± 2.8 | 8.77 ± 3.12 | 0.101 ± 0.013 |
| S11-$A_g$ (O) | 425.2 | 419.7 | 5.2 | 426.1 ± 0.8 | 0.71 ± 0.21 | –0.26 ± 0.06 | 5.2 ± 2.1 | 6.73 ± 2.07 | –0.028 ± 0.017 |
| S12-$B_g$ (O) | 473.2 | 467.7 | | 473.3 ± 3.7 | 0.60 ± 0.17 | –0.40 ± 0.16 | 9.5 ± 3.1 | 5.33 ± 3.05 | 0.075 ± 0.013 |
| S13-$A_g$ (O) | 509.6 | 501.1 | | 511.5 ± 4.8 | 1.16 ± 0.51 | –0.59 ± 0.13 | 4.3 ± 1.8 | 2.94 ± 1.37 | –0.071 ± 0.007 |
| S14-$B_g$ (O) | 527.4 | 523.1 | | 532.3 ± 1.8 | –3.37 ± 1.94 | –0.26 ± 0.21 | 10.6 ± 3.3 | 7.47 ± 2.06 | 0.172 ± 0.095 |
| S15-$B_g$ (O) | 568.9 | 534.8 | | | | | | | |
| S16-$B_g$ (O) | 659.5 | 601.1 | | 653.9 ± 5.4 | 10.89 ± 4.53 | –2.52 ± 1.25 | 18.5 ± 5.1 | 10.06 ± 3.42 | –0.536 ± 0.241 |
| S17-$A_g$ (O) | 677.8 | 651.0 | 7.2 | 686.8 ± 4.4 | –6.95 ± 3.21 | –0.43 ± 0.16 | 5.4 ± 2.7 | 13.06 ± 4.13 | –0.667 ± 0.148 |
| S18 (second order) | 1133.6 | | | | | | | | |
| S19 (second order) | 1215.9 | | | | | | | | |
| S20 (second order) | 1321.8 | | | | | | | | |

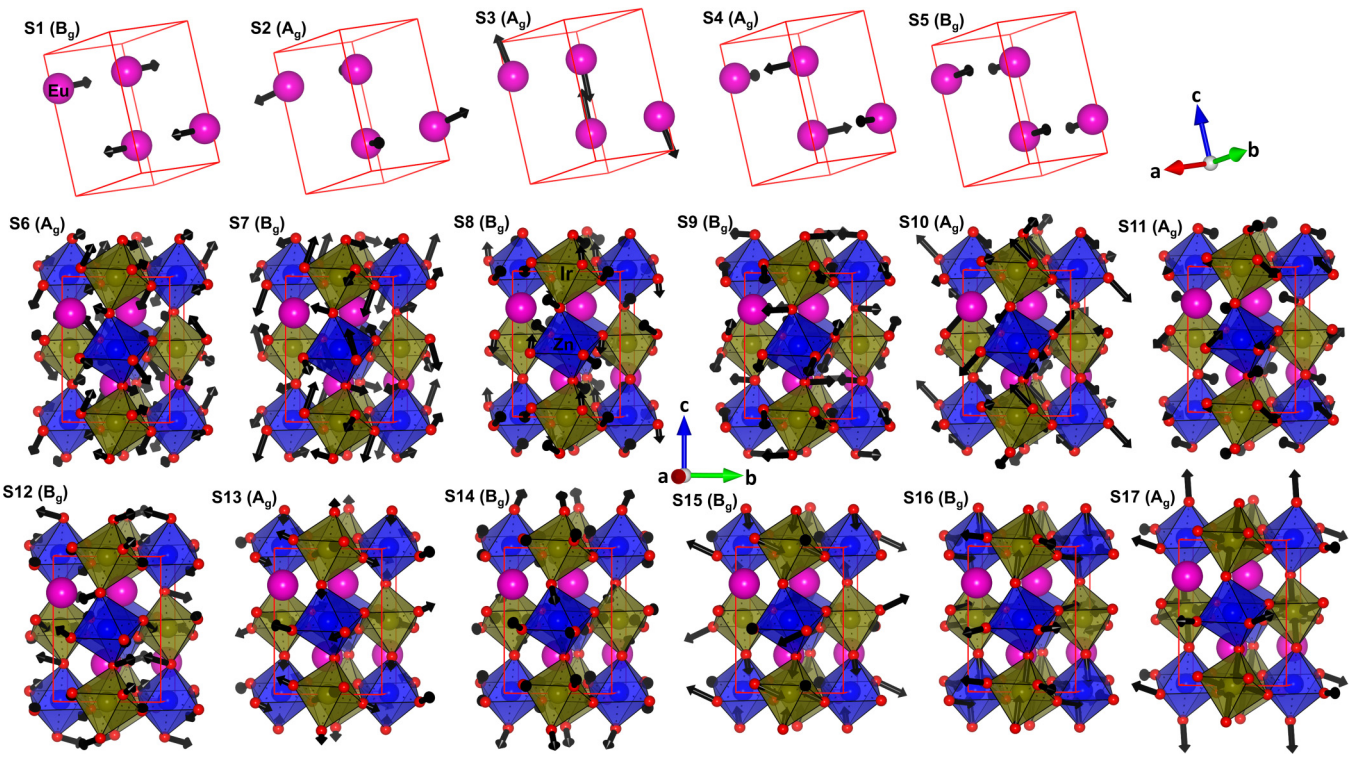


FIG. 2. Schematic representation of the eigenvectors of the first-order phonon modes S1–S17 of $Eu_2ZnIrO_6$, where pink, blue, dark yellow, and red spheres represent the Eu, Zn, Ir, and oxygen atoms, respectively. Black arrows on the atoms indicate the direction of atomic displacement, and the magnitude of the arrow illustrates the extent of atomic vibration. *a*, *b*, and *c* indicate the crystallographic axis.

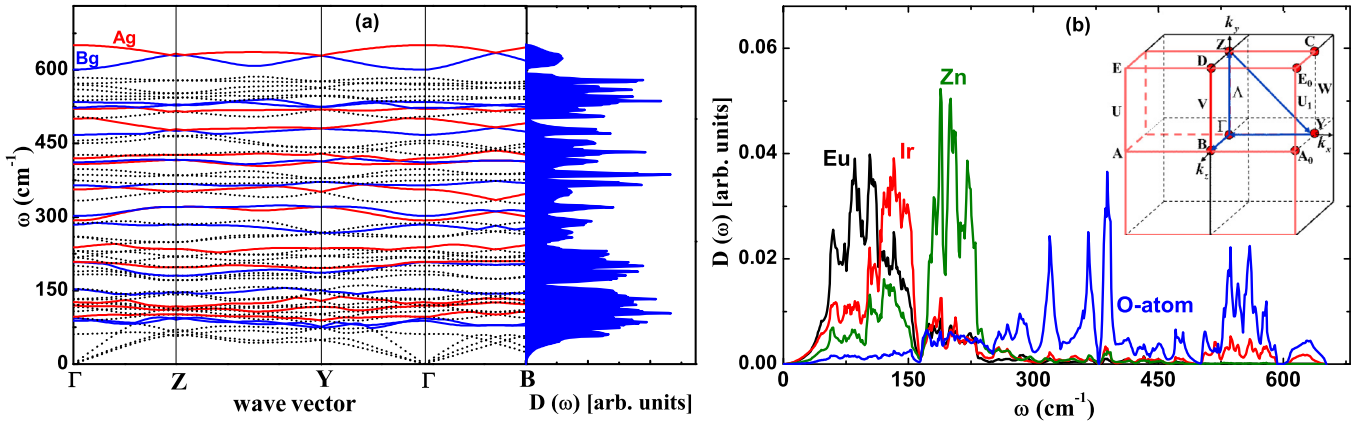


FIG. 3. (a) (Left panel) Phonon dispersion: red and blue lines represent dispersion of the Raman active $A_g$ and $B_g$ modes, respectively; broken black lines illustrate the infrared modes. (Right panel) Total phonon density of states of $Eu_2ZnIrO_6$. (b) Projected phonon density of states associated with Eu, Zn, Ir, and oxygen atoms. Inset shows first Brillouin zone along with high-symmetry path; solid blue lines indicate the path of calculated phonon dispersion.

of $Eu_2ZnIrO_6$. Figure 3(a) shows the phonon dispersion (left panel) along the $\Gamma - Z - Y - \Gamma$ high-symmetry points in the Brillouin zone, and the total phonon density of states (right panel). Figure 3(b) illustrates the projected phonon density of states [$D(\omega)$] associated with individual atoms, i.e., Eu, Zn, Ir, and oxygen atoms; the inset shows the Brillouin zone with high-symmetry points (solid blue arrows show path of the calculated phonon dispersion). We have not observed any frequency with negative sign in the phonon dispersion that emphasizes the dynamic stability of $Eu_2ZnIrO_6$. The projected phonon density of states clearly shows that the density of states at the low-frequency region is mainly dominated by heavy elements Eu, Zn, and Ir, while the high-frequency density of states is associated with the oxygen atoms. Apart from the first-order phonon modes, we observed a large number of additional modes at high energy in the spectral range of 1400–4900 $cm^{-1}$, labeled as P1–P39 shown in Fig. 1(c), attributed to the intraconfigurational transition modes of the $4f$ levels of $Eu^{3+}$ ions; the detailed discussion is presented in Secs. III C and III D.

### B. Temperature dependence of the phonon modes

In this section, we will be focusing on understanding the temperature evolution of the first- as well as second-order phonon modes. First, we will discuss the first-order phonon modes, i.e., modes below ~750 $cm^{-1}$. As the temperature is lowered, conventionally the mode frequencies are expected to show blueshift. At the same time, with decreasing temperature, anharmonic phonon-phonon interaction reduces which results in an increase of phonon lifetime or a decrease of FWHM [14]. As the linewidth of the phonon mode is related to the phonon lifetime, i.e., linewidth ($\Gamma$) $\propto$ 1/lifetime ($\tau$), the lifetime (or phonon decay time) of the different phonon modes may vary because of their different interaction channels, and is reflected in the varying linewidth. Figure 4 shows the temperature dependence of frequency and linewidth of the first-order phonon modes. The following important observations can be made: (i) Low-frequency phonon mode S1 (~71 $cm^{-1}$) exhibits nearly temperature independent behavior down to ~100 K, which gradually decreases with decrease in temperature up to ~40 K. On further lowering the temperature, mode frequency exhibits a sharp decrease down to the lowest recorded temperature, while the corresponding damping constant shows normal behavior until ~100 K, below which it exhibits a change of slope. (ii) All other phonon modes, S2, S4, S5, S8, S10, S11, and S17, exhibit normal temperature dependence down to ~40 K, i.e., increase (decrease) in the mode frequency (linewidth) with decreasing temperature, and below ~40 K these modes exhibit renormalization, i.e., anomalous phonon softening. (iii) The linewidth of the high-frequency phonon modes S8, S10, S11, and S17 exhibits line broadening at low temperature below ~40 K, while minimal line narrowing with change in slope is observed for the low-frequency phonon modes S2, S4, and S5 around this temperature. Appearance of anomaly in the phonon self-energy parameters within the spin-solid phase, i.e., long-range magnetically ordered phase, of magnetic materials is generally attributed to the entanglement of the lattice with underlying spin degrees of freedom via strong spin-phonon coupling [26,28,31,32,38].

Before discussing the origin of anomaly in the phonon self-energy parameters, we quantify the effect of anharmonicity on the phonon modes. As in a periodic crystal the potential energy expansion in the power series of atomic displacement from the equilibrium position is limited to the harmonic approximation at absolute zero, and is exactly solvable in terms of the normal modes of lattice vibrations popularly known as the linear harmonic oscillator. However, at any finite temperature the harmonic approximation cannot explain the properties of a real crystal, and needs to go beyond the harmonic approximation. Therefore, the higher-order terms are involved in the crystal potentials given as $U(r) = U(r_0) + r\frac{\partial U}{\partial r}|_{r=r_0} + r^2\frac{\partial^2 U}{\partial r^2}|_{r=r_0} + r^3\frac{\partial^3 U}{\partial r^3}|_{r=r_0} + \cdots$, where the first term is constant, and second term will go to zero under an equilibrium configuration. Also, the third term is pure harmonic in nature, and therefore does not contribute to the temperature dependence of phonon modes [39]. Hence, the anharmonicity of the phonon mode is attributed to the cubic- and higher-order terms in the crystal potential, and is

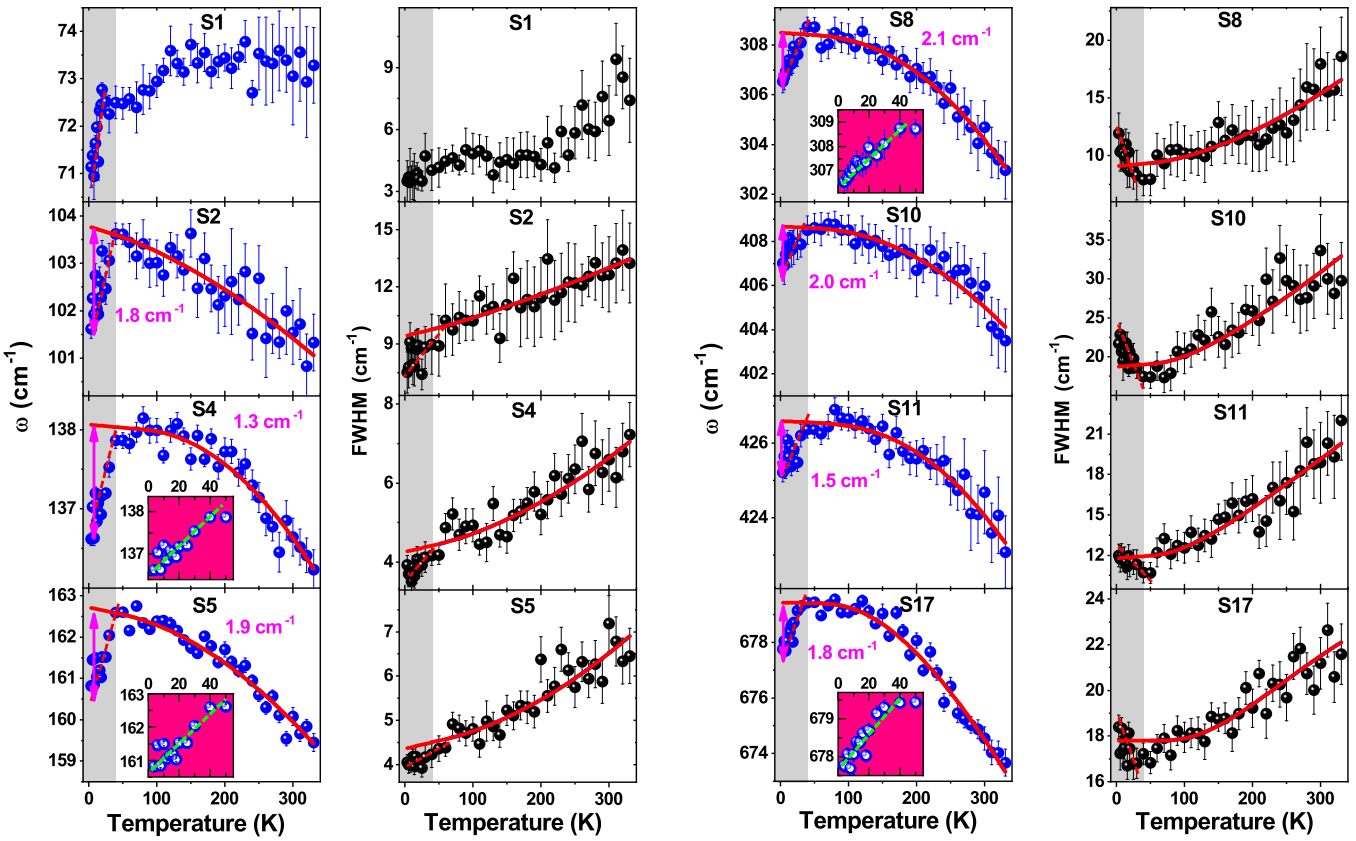


FIG. 4. Temperature dependence of the frequency and linewidth of prominent first-order phonon modes of $Eu_2ZnIrO_6$ (Inset: S4, S5, S8, and S17 show the zoomed view below 55 K and broken green lines are a guide to the eye). Solid red lines in the temperature range of 40–330 K are the fitted curves as described in the text and red lines below 40 K are the extrapolated curves. The shaded part depicts the magnetically ordered phase and broken red lines are a guide to the eye.

written as $U_{anh}(r) = gr^3 + mr^4 + \cdots \equiv \beta(a^+a^+a + a^+aa) + \gamma(a^+a^+a^+a + a^+a^+aa) + \cdots$ where $a^+$, $a$ represents the phonon creation and annihilation operator, respectively. The cubic term ($gr^3$) corresponds to the decay of an optical phonon mode into two phonons of equal frequency, i.e., $\omega_1 = \omega_2 = \frac{\omega_o}{2}$, known as cubic anharmonicity, and the quartic term ($mr^4$) in the crystal potential leads to decay of an optical phonon mode into three phonons of equal frequency, i.e., $\omega_1 = \omega_2 = \omega_3 = \frac{\omega_o}{3}$, known as quadratic anharmonicity [14,40,41]. The effect of anharmonicity on the phonon modes' frequency and linewidth in the temperature range of 40–330 K is determined fitting with the anharmonic phonon-phonon interaction model, given as [41]

$$\omega(T) = \omega_o + A\left(1+\frac{2}{e^x-1}\right) + B\left(1+\frac{3}{e^y-1}+\frac{3}{(e^y-1)^2}\right), \quad (1)$$

and

$$\Gamma(T) = \Gamma_o + C\left(1+\frac{2}{e^x-1}\right) + D\left(1+\frac{3}{e^y-1}+\frac{3}{(e^y-1)^2}\right), \quad (2)$$

where $\omega_o$ and $\Gamma_o$ are the mode frequency and linewidth at absolute zero temperature, respectively, and $x = \frac{\hbar\omega_o}{2k_BT}$; $y = \frac{\hbar\omega_o}{3k_BT}$, while $A$, $B$, $C$, and $D$ are constants. The parameters obtained from fitting are summarized in Table II. We notice that the obtained values of constant parameters $A$ and $C$ are linked to three-phonon anharmonic decay processes, which dominate for all the observed phonon modes. Solid red lines in the temperature range of 40–330 K represent the anharmonic model fit to the experimental data and red solid lines below 40 K are the curve plotted using the linear extrapolation method (see Fig. 4). Considering the anharmonic phonon-phonon interaction picture, the linewidth is expected to be higher with the increasing phonon energy, as also observed here (see Fig. 4). Such increase in the linewidth with increased phonon energy may be understood by the availability of more decay paths into phonons with equal and opposite wave vector. The lowest observed phonon mode (S1) has only an acoustic phonon mode channel to decay into and hence it is the sharpest, but higher-energy modes will have the decay channel of all the available lower-energy phonons including the acoustic one, and hence are broader.

Phonon-phonon anharmonic model fits are in very good agreement with the observed change in the frequencies and linewidths in the temperature range of 40–330 K hinting that temperature evolution in this temperature is mainly governed by the lattice degrees of freedom. However, we noticed a pronounced deviation of the frequencies and linewidths of the phonon modes from the curve estimated by anharmonic phonon-phonon interaction model at low temperature below ~40 K, indicating that this behavior cannot be described within this anharmonic phonon-phonon interaction picture. For phonons in the spin-solid phase below $T_N$, an additional decay channel is expected into pairs of magnons of equal

and opposite wave vector. These observed anomalies below ∼40 K may be understood by taking into account the interaction of phonons with the underlying magnetic degrees of freedom.

The change in the phonon frequency due to interaction of the lattice with spin degrees of freedom is given as [42] $\Delta\omega \approx \omega_{sp}(T) - \omega_o(T) = \lambda_{sp}\langle S_i S_j\rangle$, where $\omega_o(T)$ corresponds to the bare phonon frequency, i.e., phonon frequency without spin-phonon coupling; $\lambda_{sp}$ ($=\frac{\partial^2 J_{ij}}{\partial u^2}$, where $J_{ij}$ is the superexchange coupling integral) is the spin-phonon coupling coefficient, which may be positive or negative, and is distinct for each phonon mode, and $\langle S_i S_j\rangle$ is the scalar spin-spin correlation function. The spin-spin correlation function is related to the order parameter $\Phi(T)$, and within the mean field theory the $\langle S_i S_j\rangle$ is given as $\langle S_i S_j\rangle = -S^2\Phi(T)$; therefore the phonon frequency deviation ($\Delta\omega$) due to spin-phonon coupling becomes [43]

$$\Delta\omega = -\lambda_{sp} S^2 \Phi(T), \tag{3}$$

where $S$ is the spin on the magnetic ion (here, we have taken $S$ ($J_{\text{eff}}$; pseudospin) $= 1/2$, for the $Ir^{4+}$ ion), and the order parameter ($\Phi$) is given as $\Phi(T) = 1 - (\frac{T}{T_N^*})^{\gamma}$, where $\gamma$ is a critical exponent. Here, we have kept $T_N^*$ as a variable instead of keeping its value fixed, i.e., ∼12 K obtained via transport measurements because we do see significant mode renormalization well above the spin-solid phase (∼12 K). The estimated value of the spin-phonon coupling constant obtained via fitting phonon frequency deviation ($\Delta\omega$) with Eq. (3) for the prominent phonon modes is tabulated in Table II. The highest obtained value of the spin-phonon coupling constant is $\sim 8\,\text{cm}^{-1}$. This large value of the spin-phonon coupling constant indicates the strong coupling of the lattice with spin degrees of freedom. However, the observation of anomalous phonon softening and linewidth broadening/narrowing well above the long-range magnetic ordering temperature ($T_N \sim 12$ K) suggests the presence of short-range spin-spin correlations deep into the paramagnetic phase, and hence broken spin rotational symmetry. We also observed that low-energy phonon modes show continuous linewidth narrowing below ∼40 K, though with a change in slope; on the other hand, high-energy phonon modes show linewidth broadening below this temperature. This opposite behavior suggests that magnetic dispersion branches are comparable or higher in energy than these low-energy phonons, and hence these additional decay channels are mostly available only to the higher-energy phonons to decay into, which showed linewidth broadening. The magnetoelastic coupling may also result in the renormalization of phonon modes at the low temperature. However, we note that the phonon frequency decreases with varying amplitude for almost all the observed modes below ∼30–40 K, hinting that if this was a purely magnetoelastic effect then the decrease in phonon frequency means an increase in the interatomic distances (as roughly $\omega \propto 1/r^{2/3}$). The increase in the interatomic distance may result in weak interaction between the atoms, and as a consequence will quench the phonon anharmonicity; i.e., phonons would decay slowly and hence the linewidth would be expected to decrease [as linewidth ($\Gamma$) $\propto 1/$lifetime ($\tau$)]. However, opposite to what is expected for a purely magnetoelastic effect we see phonon modes with linewidth broadening (see modes S8, S10, S11, and S17 in Fig. 4) below ∼30–40 K, suggesting the dominant role of spin-phonon coupling. We hope that our studies will inspire a detailed theoretical study of magnetic dispersion in these systems to quantitively understand these anomalies.

This section will discuss the origin of the high-frequency phonon modes (i.e., S18–S20) observed in the frequency range of 1000–1400 $\text{cm}^{-1}$. Considering the frequency range of these modes and the fact that these are much above the observed first-order phonon modes' limiting frequency (∼700 $\text{cm}^{-1}$), these modes are attributed to the second-order phonon modes corresponding to the S15–S17 first-order modes. Their origin in the intraconfigurational transitions of the $Eu^{3+}$ ion is ruled out as they are also observed at the same position (i.e., Raman shift) with a different excitation laser, i.e., 633 nm. Second-order phonon modes are generally broader than their first-order counterparts because they involve the phonons over the entire Brillouin zone with a major contribution from the region of higher density of states. Specifically, the breadth of a second-order Raman band is governed by the dispersion of the first-order phonon modes; also, their peak frequencies are not necessarily double those of the first-order phonons at the gamma point. They may also result from the combination of two first-order modes depending on the symmetry. In correlated systems, generally the higher-order mode intensity goes as $g^{*n}$, where $g$ is the electron-phonon coupling constant, and is less than 1, and $n$ is the order of phonons; therefore generally higher-order phonons are also expected to be of lower intensity as compared to the corresponding first-order modes. We have assigned the second-order modes S18–S20 as the overtone of the first-order modes S15–S17, respectively. We note that these second-order modes may also be assigned as a possible combination of the different first-order modes; for example, S20 may be assigned as combination of S16 and S17. Figure 5 shows the temperature evolution of the peak frequency, FWHM, and intensity of the prominent second-order mode, i.e., S20. The following observations can be made: (i) Mode frequency and linewidth show normal temperature dependence, i.e., increase (decrease) in frequency (FWHM) with decreasing temperature, and the intensity shows an anomalous increase with decreasing temperature. The observed increase in intensity may arise because of the increased resonance effect with decreasing temperature. The change in the frequency of mode S20 ($\Delta\omega \sim 12\,\text{cm}^{-1}$) is almost double that of the first-order mode S17 ($\Delta\omega \sim 6\,\text{cm}^{-1}$) in the entire temperature range, and the linewidth at low temperature is more than double the linewidth of mode S17.

### C. Intraconfigurational modes of $Eu^{3+}$ in $Eu_2ZnIrO_6$

Apart from the first- and second-order phonon modes, we observed a large number of modes in the spectral range of 1400–4900 $\text{cm}^{-1}$ [see Figs. 1(a) and 1(c)]. Modes P1–P39 in the spectral range of 1400–4900 $\text{cm}^{-1}$ are attributed to the intraconfigurational electronic transitions of $4f$ levels of $Eu^{3+}$ ions in $Eu_2ZnIrO_6$, where $Eu^{3+}$ ions occupy $C_1$ local site symmetry surrounded by eight oxygen atoms. Because of the $C_1$ local site symmetry, the degeneracy of the free-ion levels of Eu is completely lifted, so that $(2J + 1)$ levels are expected

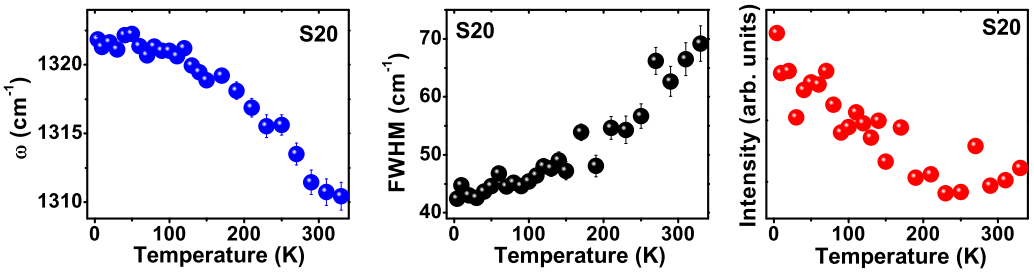


FIG. 5. Temperature dependence of frequency, linewidth, and intensity of prominent second-order phonon (S20) mode of $Eu_2ZnIrO_6$.

for each $J$ term. Figure 6(a) shows the temperature evolution of these intraconfigurational modes in the temperature range of 4–330 K excited with a 532-nm laser. In the $Eu^{3+}$ ion, the ground state $^7F_J$ is well separated from the excited states $^5D_J$; as a result the transitions can be assigned by keeping $J$ as a good quantum number. The observed set of spectral lines in the absolute energy range of 17 500–13 800 cm$^{-1}$ is attributed to the transitions from the first excited state ($^5D_0$) to the ground state $^7F_J$ ($J = 0$, 1, 2, 3, and 4) multiplets of the $Eu^{3+}$ ion [see Fig. 6(a)]. We have assigned the spectral band centered around [in absolute energy scale; see Fig. 6(a)] ∼17 200 cm$^{-1}$ (P1–P3), 16 800 cm$^{-1}$ (P4–P11), 16 100 cm$^{-1}$ (P12–P20), 15 250 cm$^{-1}$ (P21–P29), and 14 150 cm$^{-1}$ (P30–P39) as transition from the high-energy $^5D_0$ level to $^7F_0$, $^7F_1$, $^7F_2$, $^7F_3$, and $^7F_4$, respectively (see the schematic representation of the energy levels [44,45] of the $Eu^{3+}$ ion, Fig. 6(b)). Raman active excitations are independent of the incident photon energy, and appear at the same position in the Raman shift even with the different energy of the excitation source. On the other hand, the emission or absorption peak position is shifted equal to the separation between the two incident laser energies, whereas their absolute position in energy remains the same. To confirm the electronic origin of these high-energy modes, we excited the spectrum using a 633-nm laser [see inset of Fig. 6(a)], and only the modes below ∼1400 cm$^{-1}$ are observed at the same position in Raman shift (not shown here), confirming the electronic transition origin of the high-energy modes (P1–P39). However, the spectrum [see inset of Fig. 6(a)] is very weak and shows a band around ∼14 100 cm$^{-1}$ (absolute energy scale) corresponding to the $^5D_0 \rightarrow {}^7F_4$ transition. The observed feeble intensity of the electronic modes using 633 nm (15 803 cm$^{-1}$) may be because the laser energy is much below (∼1500 cm$^{-1}$) the first excited state $^5D_0$ (∼17 300 cm$^{-1}$) energy, and to have transition from the first excited state to the ground state it needs the phonon absorption of the energy scale of ∼1500 cm$^{-1}$.

We note that the intensity of $^5D_0 \rightarrow {}^7F_J$ transition bands is remarkably quenched with decreasing temperature [see inset

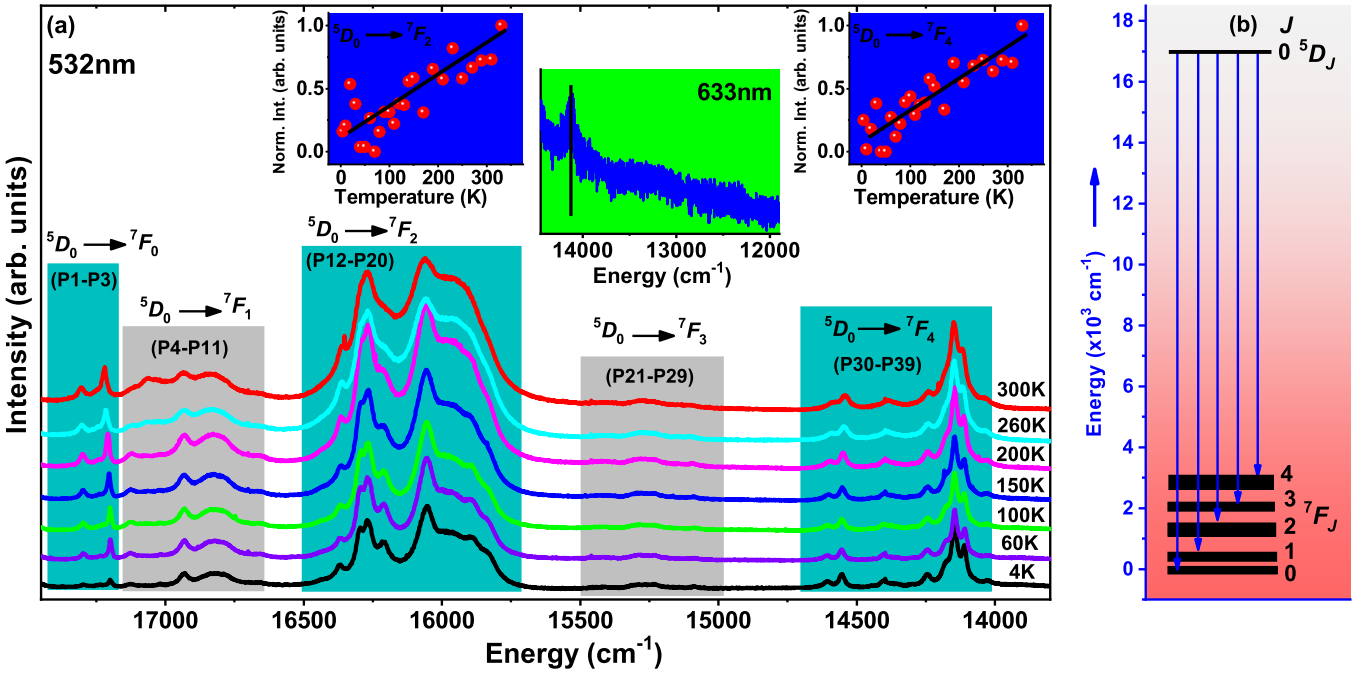


FIG. 6. (a) Temperature evolution of the high-energy spectra of intraconfigurational modes of $Eu^{3+}$ ions in the absolute energy range of 18 500–13 500 cm$^{-1}$. Inset shows the spectra excited with a 633-nm laser, and the temperature dependence of the intensity of $^5D_0 \rightarrow {}^7F_2$ and $^5D_0 \rightarrow {}^7F_4$ transition bands (solid black line is a guide to the eye). (b) The schematic representation of the crystal-field splitting of energy levels of the $Eu^{3+}$ ion. Vertical blue lines indicate the observed transitions.

TABLE III. List of the frequency and linewidth of the prominent intraconfigurational transition modes of $Eu^{3+}$ in $Eu_2ZnIrO_6$, at 4 K. Units are in $cm^{-1}$.

| $^5D_0 \rightarrow {}^7F_0$ | | | $^5D_0 \rightarrow {}^7F_1$ | | | $^5D_0 \rightarrow {}^7F_2$ | | | $^5D_0 \rightarrow {}^7F_3$ | | | $^5D_0 \rightarrow {}^7F_4$ | | |
|---|---|---|---|---|---|---|---|---|---|---|---|---|---|---|
| Mode | $\omega_{abs.}$ | $\Gamma$ | Mode | $\omega_{abs.}$ | $\Gamma$ | Mode | $\omega_{abs.}$ | $\Gamma$ | Mode | $\omega_{abs.}$ | $\Gamma$ | Mode | $\omega_{abs.}$ | $\Gamma$ |
| P1 | 17296 | 18.4 | P7 | 16933 | 39.0 | P13 | 16369 | 43.6 | P24 | 15288 | 22.9 | P31 | 14554 | 22.3 |
| P3 | 17198 | 12.9 | P8 | 16868 | 53.9 | P14 | 16298 | 37.2 | P25 | 15267 | 23.0 | P32 | 14403 | 23.7 |
| | | | P9 | 16833 | 65.7 | P15 | 16266 | 36.6 | P26 | 15234 | 54.0 | P34 | 14245 | 30.2 |
| | | | P10 | 16787 | 80.7 | P16 | 16210 | 79.6 | | | | P36 | 14146 | 24.5 |
| | | | | | | P17 | 16057 | 84.1 | | | | P37 | 14111 | 23.9 |
| | | | | | | P18 | 15965 | 112.4 | | | | | | |

of Fig. 6(a) for prominent bands]. A similar decrease in the band intensity is also reported for other rare-earth based systems [45–47]. This temperature evolution of the intensity may be understood by the fact that with decreasing temperature nonradiative decay from $^5D_1$ to $^5D_0$ decreases significantly. As the incident photon energy 532 nm (18 796 $cm^{-1}$) in the present case is close to the $^5D_1$ level, by absorption of the available thermal phonons via electron-phonon coupling it may easily reach the $^5D_1$ level. However, with decreasing temperature, thermal population of the phonons decreases sharply; as a result the density of the $^5D_1$ state also decreases and so does the nonradiative decay rate to the $^5D_0$ state, which may finally result in decreased density of the $^5D_0$ state, and hence the intensity with decreasing temperature. The transition between the electronic levels may be classified as electric dipole (ED), magnetic dipole (MD), and quadrupole mediated transitions, each with a different transition rate and selection rule; the strongest rate is for the electric-dipole mediated one followed by magnetic dipole and then higher-order ones. Within the Judd-Ofelt theory the transition from $^5D_0 \rightarrow {}^7F_2$ is ED mediated and is generally the strongest [48–50]. On the other hand, $^5D_0 \rightarrow {}^7F_1$ is MD mediated and is expected to be weak. However, transition from $^5D_0 \rightarrow {}^7F_3$ is both ED and MD forbidden but higher order, such as quadrupole as well as crystal-field mixing of the levels, may contribute to these transitions; as a result these transitions are usually weak in intensity. Generally, the $^5D_0 \rightarrow {}^7F_0$ transition is not allowed except in cases where the crystal-field active ion has special symmetry such as $C_s$, $C_1$ (as in the present case), $C_2$, $C_3$, $C_4$, $C_6$, $C_{2v}$, $C_{3v}$, $C_{4v}$, and $C_{6v}$, and is expected to be weak. Interestingly, our observations evidenced that most intense transition indeed occurs from $^5D_0 \rightarrow {}^7F_2$ centered around ∼16 100 $cm^{-1}$, and transitions corresponding to the $^5D_0 \rightarrow {}^7F_{0/1/3}$ are weak in line with the theory.

The high-energy spectrum is fitted with a sum of Lorentzian functions [see Fig. 1(c)] and the extracted peak position and linewidth of the prominent modes at 4 K are tabulated in Table III. Interestingly, the linewidth of the modes in the bands corresponding to $^5D_0 \rightarrow {}^7F_{1/2/3}$ transitions shows continuous increase as one goes toward the lower-energy side, and modes corresponding to the $^5D_0 \rightarrow {}^7F_4$ transition band show a minimal increase (see Table III). This characteristic feature of the linewidth arises because of the transition to different levels of multiplets within the same crystal-field level; the narrow modes correspond to the transition to the lowest-energy level of the multiplet and the broad modes indicate the transition to the high-energy levels of the same multiplet. This behavior of the linewidth also reflects significant coupling of the lattice with electronic degrees of freedom, as the linewidth broadening is attributed to a relaxation to the available lower-energy levels via emission of the phonons [51]. We observed three modes in the energy range of the $^5D_0 \rightarrow {}^7F_0$ transition at around ∼17 300 $cm^{-1}$ (P1) and ∼17 200 $cm^{-1}$ (P3) along with a very weak shoulder mode around ∼17 235 $cm^{-1}$ (P2), at 4 K and the linewidths of the modes are noted to be sharpest in the spectrum. The observation of more than one peak in this energy range suggests the nonequivalent crystallographic sites of the $Eu^{3+}$ ion [52]. As in the case of equivalent $Eu^{3+}$ sites, only one transition is allowed due to the nondegenerate nature of the excited ($^5D_0$) and ground ($^7F_0$) state multiplets. P2 and P3, separated by ∼35 $cm^{-1}$, may be due to two equivalent sites of $Eu^{3+}$. We also observed a third peak, and it may have its origin in the transition from the $^5D_1 \rightarrow {}^7F_J$ levels. As the $^5D_0 \rightarrow {}^7F_0$ transition in the present case is allowed by the local symmetry group ($C_1$), the intensity gained by this transition band is attributed to the mixing of $^7F_0$ and $^7F_2$ crystal-field levels. The estimated intensity ratio of the bands from $^5D_0 \rightarrow {}^7F_0$ to $^5D_0 \rightarrow {}^7F_2$ is ∼0.012, which is quite high, suggesting $J$ mixing. The intensity ratio of these transitions is also related as [53,54]

$$\frac{I(^5D_0 \rightarrow {}^7F_0)}{I(^5D_0 \rightarrow {}^7F_2)} = \frac{4\left(B_0^2\right)^2}{75\left(\Delta_0^2\right)^2},$$

where $B_0^2$ is the second-order crystal-field parameter and is associated with the environment of $Eu^{3+}$ ions, and $\Delta_0^2$ corresponds to the energy difference between the $^7F_0$ and $^7F_2$ states; $\Delta_0^2 \sim 830\ cm^{-1}$ in $Eu_2ZnIrO_6$. Estimated value of the second-order crystal-field parameter is $B_0^2 \sim 394\ cm^{-1}$ (∼50 meV), which is quite high, indicating strong mixing of $^7F_0$ and $^7F_2$ levels.

### D. Temperature dependence of the intraconfigurational modes of $Eu^{3+}$ ion

Now we will discuss the temperature dependence of the energy and linewidth of the prominent high-energy modes, i.e., P1, P3, P4, P7, P14–P17, P19, P30, P32, P34, P36, and P37 as shown in Fig. 7. The following observations can be made: (i) The energies of modes P1, P3, P7, P16, P17, P19, P36, and P37 exhibit redshift with decreasing temperature. (ii) However, the energies of other intraconfigurational modes, P4, P14, P15, P30–P32, and P34, exhibit blueshift (show a similar temperature dependence as that of phonon modes)

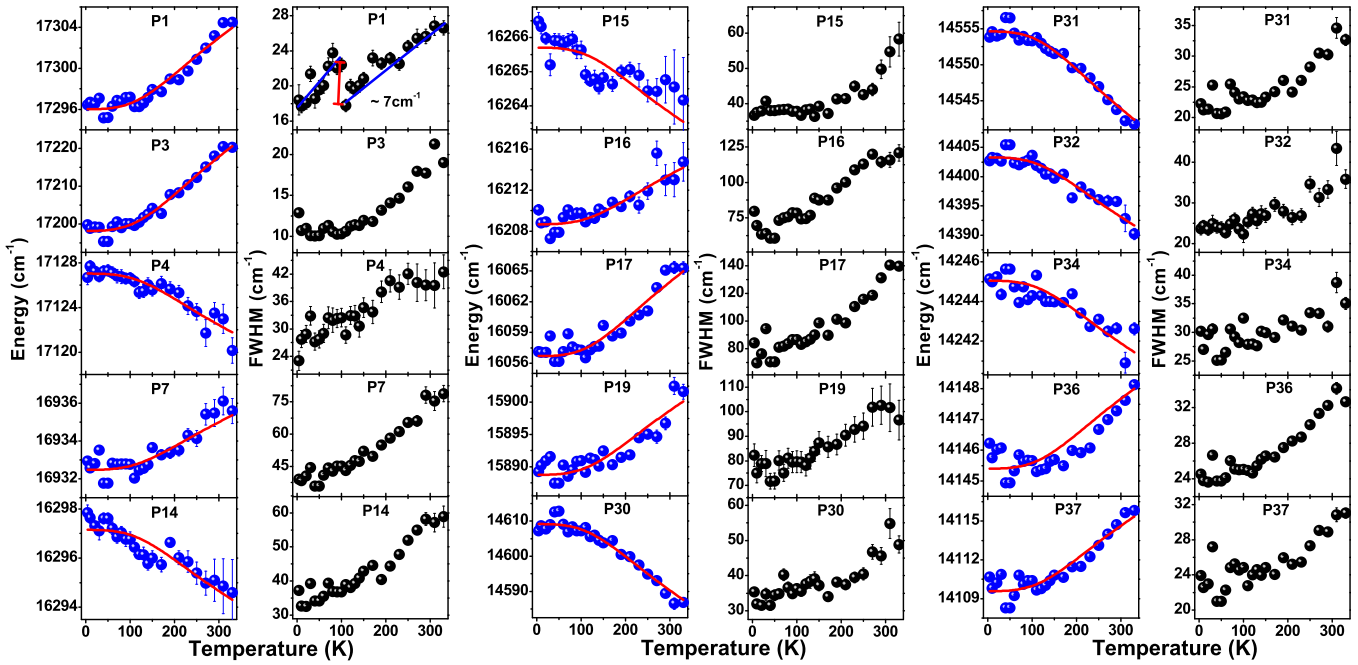


FIG. 7. Temperature dependence of energy and linewidth of the prominent high-energy intraconfigurational modes P1, P3, P4, P7, P14–P17, P19, P30–P32, P34, P36, and P37 in the temperature range of 4–330 K. Solid red lines are the fitted curves as described in the text.

with decreasing temperature down to the lowest recorded temperature 4 K. (iii) The linewidth of the $^5D_0 \rightarrow {}^7F_0$ transition mode P1 exhibits a change in slope around ∼100 K with a jump of around ∼7 $cm^{-1}$ (line broadening) that indicates a reduced lifetime of transition; a similar reduction in the lifetime of this transition is also reported in previous studies of $Eu^{3+}$ in emission decay curves, where emission decay time changes from ∼2.0 ms to ∼0.04 $\mu$s (i.e., fast decay at low temperature) [52]. (iv) The linewidth of all other intraconfigurational modes shows line narrowing with decreasing temperature. Line narrowing with decreasing temperature may occur due to the reduction of electrostatic potential at the Eu site because of reduced lattice vibrations. The surrounding ligands of the $Eu^{3+}$ ion generate a finite static potential, resulting in the so-called crystal-field interaction, and remove the degeneracy of the free-ion energy levels. In fact, at nonzero temperature, ions do move around their equilibrium position and renormalize the crystal-field interaction via phonons, and this interaction with phonons may explain the thermal dependence of the spectral linewidth and line position. Temperature dependence of the energy of intraconfigurational modes occurs due to a change in phonon frequency accompanying the optical excitation and dynamic modulation of the electronic levels by the phonons. The amount of change depends on the coupling strength of ions with the phonons. The energy shift of the intraconfigurational modes as a function of temperature is described using the Debye model of phonons within the weak ion-phonon coupling limit given as [51]

$$E_i(T) = E_i(0) + \alpha_i \left(\frac{T}{\theta_D}\right)^4 \int_0^{\theta_D/T} \frac{x^3}{e^x - 1} dx, \qquad (4)$$

where $\alpha_i = \frac{3}{2} W_i \omega_D$, $\theta_D$ is the Debye temperature (975 K here), $\omega_D$ is the Debye phonon frequency in $cm^{-1}$, and $W_i$ is the ion-phonon coupling constant. The Debye model fit to the experimental temperature dependence of mode energy is in good agreement, and the values obtained from the fit are summarized in Table IV. The majority of the observed modes are shifted toward higher energy with decreasing temperature and are fit well with Eq. (4), suggesting that the associated energy levels move downward with increasing temperature. The transition modes following the temperature-dependent behavior similar to the phonons (blueshift with decreasing temperature) unambiguously signal their phonon mediated nature. The value of the ion-phonon parameter ($W_i$) is negative for these modes; however, this value is positive for other modes showing redshift with decreasing temperature (see Table IV). The redshift of some of the observed modes with decreasing temperature may be understood by the so-called pushing effect or fast lowering of the terminal levels [55]. A similar redshift has also been reported for other rare-earth elements [23,55–57]. It has been associated with the fact that terminal levels decrease

TABLE IV. List of the parameters extracted from fitting the temperature dependence of intraconfigurational mode energies of $Eu^{3+}$ in $Eu_2ZnIrO_6$ as described in the text. The value of $\theta_D = 975$ K.

| Mode | $\omega(0)$ | $\alpha_i$ | $W_i$ | Mode | $\omega(0)$ | $\alpha_i$ | $W_i$ |
|---|---|---|---|---|---|---|---|
| P1 | 17296 | +82.6 | +0.08 | P19 | 15889 | +117.7 | +0.11 |
| P3 | 17198 | +232.6 | +0.23 | P30 | 14609 | –223.9 | –0.22 |
| P4 | 17127 | –54.6 | –0.05 | P31 | 14555 | –126.5 | –0.12 |
| P7 | 16932 | +29.9 | +0.03 | P32 | 14403 | –120.7 | –0.11 |
| P14 | 16297 | –29.5 | –0.03 | P34 | 14245 | –37.4 | –0.04 |
| P15 | 16266 | –22.5 | –0.02 | P36 | 14145 | +26.9 | +0.03 |
| P16 | 16209 | +57.4 | +0.06 | P37 | 14109 | +59.8 | +0.06 |
| P17 | 16057 | +85.8 | +0.06 | | | | |

faster than other levels with increasing temperature; therefore transition from a higher level to these terminal levels of any set of multiplets will result in the redshift. More theoretical work is required to understand these redshifts and their coupling with other quasiparticles.

## IV. SUMMARY AND CONCLUSIONS

To summarize, we report the detailed lattice-dynamics study of double-perovskite $Eu_2ZnIrO_6$ via Raman scattering as a function of temperature and density functional theory based calculations. We find significant phonon softening and anomalous linewidth narrowing/broadening of the phonon modes well above the spin-solid phase ($T_N \sim 12$ K) up to ~40 K. Our study foretells that the quantum magnetic ground state of $5d$ iridium based double-perovskite materials is the result of intricate coupling of lattice, spin, and electronic degrees of freedom, suggesting that these degrees of freedom should be treated at par with each other to write the ground-state Hamiltonian for their understanding. The estimated value of the spin-phonon coupling constant ($\lambda_{sp}$) is found to range from ~5 to 8 $cm^{-1}$. The high value of the second-order crystal-field parameter, $B_0^2 \sim 50$ meV, suggests strong $J$ mixing of the crystal-field split levels of the $Eu^{3+}$ ion. The density functional theory based calculated zone-centered phonon mode frequencies are observed to be in very good agreement with the experimentally observed values. Our lattice-dynamics studies reveal the rich physics associated with optical phonons and their coupling to electronic and magnetic degrees of freedom in this system. We believe that our studies will motivate further theoretical work for the estimation of all possible intraconfigurational transitions of $4f$ levels of $Eu^{3+}$ in $C_1$ low-symmetry configuration as well as aid in quantitatively understanding the coupling between these different degrees of freedom and their contribution to the ground state.

## ACKNOWLEDGMENTS

P.K. thanks the Department of Science and Technology, India, for the grant and IIT Mandi for the experimental facilities. The authors in Dresden thank Deutsche Forschungsgemeinschaft (DFG) for financial support via Grant No. DFG AS 523/4-1 (S.A.) and via Project No. B01 of SFB 1143 (Project ID No. 247310070).

[1] B. J. Kim, H. Jin, S. J. Moon, J.-Y. Kim, B.-G. Park, C. S. Leem, J. Yu, T. W. Noh, C. Kim, S.-J. Oh, J.-H. Park, V. Durairaj, G. Cao, and E. Rotenberg, Novel $J_{\rm eff} = 1/2$ Mott State Induced by Relativistic Spin-Orbit Coupling in $Sr_2IrO_4$, Phys. Rev. Lett. **101**, 076402 (2008).

[2] B. J. Kim, H. Ohsumi, T. Komesu, S. Sakai, T. Morita, H. Takagi, and T. Arima, Phase-sensitive observation of a spin-orbital Mott state in $Sr_2IrO_4$, Science **323**, 1329 (2009).

[3] H. Watanabe, T. Shirakawa, and S. Yunoki, Microscopic Study of a Spin-Orbit-Induced Mott Insulator in Ir Oxides, Phys. Rev. Lett. **105**, 216410 (2010).

[4] Y. Yamaji, Y. Nomura, M. Kurita, R. Arita, and M. Imada, First-Principles Study of the Honeycomb-Lattice Iridates $Na_2IrO_3$ in the Presence of Strong Spin-Orbit Interaction and Electron Correlations, Phys. Rev. Lett. **113**, 107201 (2014).

[5] C. Dhital, T. Hogan, W. Zhou, X. Chen, Z. Ren, M. Pokharel, Y. Okada, M. Heine, W. Tian, Z. Yamani, C. Opeil, J. S. Helton, J. W. Lynn, Z. Wang, V. Madhavan, and S. D. Wilson, Carrier localization and electronic phase separation in a doped spin-orbit-driven Mott phase in $Sr_3(Ir_{1-x}Ru_x)_2O_7$, Nat. Commun. **5**, 3377 (2014).

[6] G. Cao, T. F. Qi, L. Li, J. Terzic, S. J. Yuan, L. E. DeLong, G. Murthy, and R. K. Kaul, Novel Magnetism of $Ir^{5+}(5d^4)$ Ions in the Double Perovskite $Sr_2YIrO_6$, Phys. Rev. Lett. **112**, 056402 (2014).

[7] H. Gretarsson, N. H. Sung, M. Höppner, B. J. Kim, B. Keimer, and M. Le Tacon, Two-Magnon Raman Scattering and Pseudospin-Lattice Interactions in $Sr_2IrO_4$ and $Sr_3Ir_2O_7$, Phys. Rev. Lett. **116**, 136401 (2016).

[8] Y. Cao, Q. Wang, J. A. Waugh, T. J. Reber, H. Li, X. Zhou, S. Parham, S.-R. Park, N. C. Plumb, E. Rotenberg, A. Bostwick, J. D. Denlinger, T. Qi, M. A. Hermele, G. Cao, and D. S. Dessau, Hallmarks of the Mott-metal crossover in the hole-doped pseudospin-1/2 Mott insulator $Sr_2IrO_4$, Nat. Commun. **7**, 11367 (2016).

[9] S. Kanungo, K. Mogare, B. Yan, M. Reehuis, A. Hoser, C. Felser, and M. Jansen, Weak orbital ordering of Ir $t_{2g}$ states in the double perovskite $Sr_2CeIrO_6$, Phys. Rev. B **93**, 245148 (2016).

[10] M. Nakayama, T. Kondo, Z. Tian, J. J. Ishikawa, M. Halim, C. Bareille, W. Malaeb, K. Kuroda, T. Tomita, S. Ideta, K. Tanaka, M. Matsunami, S. Kimura, N. Inami, K. Ono, H. Kumigashira, L. Balents, S. Nakatsuji, and S. Shin, Slater to Mott Crossover in the Metal to Insulator Transition of $Nd_2Ir_2O_7$, Phys. Rev. Lett. **117**, 056403 (2016).

[11] L. T. Corredor, G. Aslan-Cansever, M. Sturza, K. Manna, A. Maljuk, S. Gass, T. Dey, A. U. B. Wolter, O. Kataeva, A. Zimmermann, M. Geyer, C. G. F. Blum, S. Wurmehl, and B. Büchner, Iridium double perovskite SrYIrO: A combined structural and specific heat study, Phys. Rev. B **95**, 064418 (2017).

[12] A. A. Aczel, J. P. Clancy, Q. Chen, H. D. Zhou, D. Reig-i-Plessis, G. J. MacDougall, J. P. C. Ruff, M. H. Upton, Z. Islam, T. J. Williams, S. Calder, and J.-Q. Yan, Revisiting the Kitaev material candidacy of $Ir^{4+}$ double perovskite iridates, Phys. Rev. B **99**, 134417 (2019).

[13] T. Dey, A. Maljuk, D. V. Efremov, O. Kataeva, S. Gass, C. G. F. Blum, F. Steckel, D. Gruner, T. Ritschel, A. U. B. Wolter, J. Geck, C. Hess, K. Koepernik, J. van den Brink, S. Wurmehl, and B. Büchner, $Ba_2YIrO_6$: A cubic double perovskite material with $Ir^{5+}$ ions, Phys. Rev. B **93**, 014434 (2016).

[14] B. Singh, G. A. Cansever, T. Dey, A. Maljuk, S. Wurmehl, B Büchner, and P. Kumar, Orbiton-phonon coupling in $Ir^{5+}(5d^4)$ double perovskite $Ba_2YIrO_6$, J. Phys.: Condens. Matter **31**, 065603 (2019).

[15] Q. Chen, C. Svoboda, Q. Zheng, B. C. Sales, D. G. Mandrus, H. D. Zhou, J.-S. Zhou, D. McComb, M. Randeria, N. Trivedi,

and J.-Q. Yan, Magnetism out of antisite disorder in the $J = 0$ compound $Ba_2YIrO_6$, Phys. Rev. B **96**, 144423 (2017).

[16] S. Fuchs, T. Dey, G. A.-Cansever, A. Maljuk, S. Wurmehl, B. Büchner, and V. Kataev, Unraveling the Nature of Magnetism of the $5d^4$ Double Perovskite $Ba_2YIrO_6$, Phys. Rev. Lett. **120**, 237204 (2018).

[17] G. Cao, A. Subedi, S. Calder, J.-Q. Yan, J. Yi, Z. Gai, L. Poudel, D. J. Singh, M. D. Lumsden, A. D. Christianson, B. C. Sales, and D. Mandrus, Magnetism and electronic structure of $La_2ZnIrO_6$ and $La_2MgIrO_6$: Candidate $J_{\rm eff} = 1/2$ Mott insulators, Phys. Rev. B **87**, 155136 (2013).

[18] K. Manna, R. Sarkar, S. Fuchs, Y. A. Onykiienko, A. K. Bera, G. A. Cansever, S. Kamusella, A. Maljuk, C. G. F. Blum, L. T. Corredor, A. U. B. Wolter, S. M. Yusuf, M. Frontzek, L. Keller, M. Iakovleva, E. Vavilova, H.-J. Grafe, V. Kataev, H.-H. Klauss, D. S. Inosov *et al.*, Noncollinear antiferromagnetism of coupled spins and pseudospins in the double perovskite $La_2CuIrO_6$, Phys. Rev. B **94**, 144437 (2016).

[19] B. Singh, D. Kumar, K. Manna, A. K. Bera, G. A. Cansever, A. Maljuk, S. Wurmehl, B. Büchner, and P. Kumar, Correlated paramagnetism and interplay of magnetic and phononic degrees of freedom in $3d$-$5d$ coupled $La_2CuIrO_6$, J. Phys.: Condens. Matter **31**, 485803 (2019).

[20] A. A. Aczel, A. M. Cook, T. J. Williams, S. Calder, A. D. Christianson, G.-X. Cao, D. Mandrus, Y.-B. Kim, and A. Paramekanti, Highly anisotropic exchange interactions of $j_{\rm eff} = 1/2$ iridium moments on the fcc lattice in $La_2BIrO_6$ ($B$ = Mg, Zn), Phys. Rev. B **93**, 214426 (2016).

[21] X. Ding, B. Gao, E. Krenkel, C. Dawson, J. C. Eckert, S.-W. Cheong, and V. Zapf, Magnetic properties of double perovskite $Ln_2CoIrO_6$ ($Ln$ = Eu, Tb, Ho): Hetero-tri-spin $3d$-$5d$-$4f$ systems, Phys. Rev. B **99**, 014438 (2019).

[22] B. Singh, M. Vogl, S. Wurmehl, S. Aswartham, B. Büchner, and P. Kumar, Kitaev magnetism and fractionalized excitations in double perovskite $Sm_2ZnIrO_6$, Phys. Rev. Res. **2**, 013040 (2020).

[23] B. Singh, M. Vogl, S. Wurmehl, S. Aswartham, B. Büchner, and P. Kumar, Kramers doublets, phonons, crystal-field excitations, and their coupling in $Nd_2ZnIrO_6$, Phys. Rev. Res. **2**, 023162 (2020).

[24] M. Vogl, R. Morrow, A. A. Aczel, R. B. Rodriguez, A. U. B. Wolter, S. Wurmehl, S. Aswartham, and B. Büchner, Complex magnetic properties in the mixed $4f$−$5d$ double perovskite iridates $X_2ZnIrO_6$ ($X$ = Nd, Sm, Eu, Gd), Phys. Rev. Mater. **4**, 054413 (2020).

[25] Y. Takikawa, S. Ebisu, and S. Nagata, Van Vleck paramagnetism of the trivalent Eu ions, J. Phys. Chem. Solids **71**, 1592 (2010).

[26] P. Kumar, A. Bera, D. V. S. Muthu, S. N. Shirodkar, R. Saha, A. Shireen, A. Sundaresan, U. V. Waghmare, A. K. Sood, and C. N. R. Rao, Coupled phonons, magnetic excitations, and ferroelectricity in $AlFeO_3$: Raman and first-principles studies, Phys. Rev. B **85**, 134449 (2012).

[27] P. Kumar, D. V. S. Muthu, L. Harnagea, S. Wurmehl, B. Büchner, and A K Sood, Phonon anomalies, orbital-ordering and electronic Raman scattering in iron-pnictide $Ca(Fe_{0.97}Co_{0.03})_2As_2$: Temperature-dependent Raman study, J. Phys.: Condens. Matter **26**, 305403 (2014).

[28] M. G. Cottam and D. J. Lockwood, *Light Scattering in Magnetic Solids* (Wiley, New York, 1986).

[29] M. Cardona, in *Light Scattering in Solids III, Topics in Applied Physics*, edited by M. Cardona and G. Guntherdot (Springer, Berlin, 1982).

[30] P. Kumar, K. P. Ramesh, and D. V. S. Muthu, Evidence for phase transitions and pseudospin phonon coupling in $K_{0.9}(NH_4)_{0.1}H_2AsO_4$, AIP Adv. **5**, 037135 (2015).

[31] B. Singh, S. Kumar, and P. Kumar, Broken translational and rotational symmetries in $LiMn_{1.5}Ni_{0.5}O_4$ spinel, J. Phys.: Condens. Matter **31**, 395701 (2019).

[32] P. Kumar, A. Kumar, S. Saha, D. V. S. Muthu, J. Prakash, S. Patnaik, U. V. Waghmare, A. K. Ganguli, and A. K. Sood, Anomalous Raman scattering from phonons and electrons of superconducting $FeSe_{0.82}$, Solid State Commun. **150**, 557 (2010).

[33] P. Rovillain, M. Cazayous, Y. Gallais, A. Sacuto, M-A. Measson, and H. Sakata, Magnetoelectric excitations in multiferroic $TbMnO_3$ by Raman scattering, Phys. Rev. B **81**, 054428 (2010).

[34] E. M. Motoyama, G. Yu, I. M. Vishik, O. P. Vajk, P. K. Mang, and M. Greven, Spin correlations in the electron-doped high-transition-temperature superconductor $Nd_{2-x}Ce_xCuO_{4\pm\delta}$, Nature **445**, 186 (2007).

[35] P. Giannozzi, S. Baroni, N. Bonini, M. Calandra, R. Car, C. Cavazzoni, D. Ceresoli, G. L. Chiarotti, M. Cococcioni, I. Dabo *et al.*, QUANTUM ESPRESSO: A modular and open-source software project for quantum simulations of materials, J. Phys.: Condens. Matter **21**, 395502 (2009).

[36] J. P. Perdew, A. Ruzsinszky, G. I. Csonka, O. A. Vydrov, G. E. Scuseria, L. A. Constantin, X. Zhou, and K. Burke, Restoring the Density-Gradient Expansion for Exchange in Solids and Surfaces, Phys. Rev. Lett. **100**, 136406 (2008).

[37] P. Giannozzi, S. de Gironcoli, P. Pavone, and S. Baroni, *Ab initio* calculation of phonon dispersions in semiconductors, Phys. Rev. B **43**, 7231 (1991).

[38] M. G. Cottam and D. J. Lockwood, Spin-phonon interaction in transition-metal difluoride antiferromagnets: Theory and experiment, Low Temp. Phys. **45**, 78 (2019).

[39] N. W. Ashcroft and N. D. Mermin, *Solid State Physics* (Holt-Saunders International Editions, Philadelphia, 1976).

[40] P. G. Klemens, Anharmonic decay of optical phonons, Phys. Rev. **148**, 845 (1966).

[41] M. Balkanski, R. F. Wallis, and E. Haro, Anharmonic effects in light scattering due to optical phonons in silicon, Phys. Rev. B **28**, 1928 (1983).

[42] D. J. Lockwood and M. G. Cottam, The spin-phonon interaction in $FeF_2$ and $MnF_2$ studied by Raman spectroscopy, J. Appl. Phys. **64**, 5876 (1988).

[43] C.-H. Hung, P.-H. Shih, F.-Y. Wu, W.-H. Li, S. Y. Wu, T. S. Chan, and H.-S. Sheu, Spin-phonon coupling effects in antiferromagnetic $Cr_2O_3$ nanoparticles, J. Nanosci. Nanotechnol. **10**, 4596 (2010).

[44] S. Taboada, A. de Andrés, and R. Sáez-Puche, Excitation and desexcitation processes of $Eu^{3+}$ luminescence in $Eu_2BaZnO_5$, J. Alloys Compd. **275-277**, 279 (1998).

[45] S. Taboada, A. de Andrés, and J. E. Munoz-Santiuste, Reflectance, luminescence and Raman experiments on

$Eu^{3+}$ crystal field transitions in $Eu_2BaZnO_5$, J. Phys.: Condens. Matter. **10**, 8983 (1998).

[46] S. Taboada, J. E. Munoz-Santiuste, and A. de Andrés, Excitation and relaxation processes of $Eu^{3+}$ crystal field transitions in $Eu_2BaZnO_5$, J. Lumin. **72-74**, 273 (1997).

[47] G. Blasse, *Solid State Luminescence: Theory, Materials and Devices*, edited by A. H. Kitai (Chapman and Hall, London, 1993).

[48] B. R. Judd, Optical absorption intensities of rare-earth ions, Phys. Rev. **127**, 750 (1962).

[49] G. S. Ofelt, Intensities of crystal spectra of rare-earth ions, J. Chem. Phys. **37**, 511 (1962).

[50] X. Y. Chen and G.K. Liu, The standard and anomalous crystal-field spectra of $Eu^{3+}$, J. Solid State Chem. **178**, 419 (2005).

[51] S. Hüfner, *Optical Spectra of Transparent Rare Earth Compounds* (Academic Press, New York, 1978).

[52] Y. Huang, H. Lin, and H. Jin Seo, Luminescence properties and local structures of $Eu^{3+}$ in $EuBaB_9O_{16}$ crystal, J. Electrochem. Soc. **157**, J405 (2010).

[53] S. Ray, P. Pramanik, A. Singha, and A. Roya, Optical properties of nanocrystalline $Y_2O_3$ : $Eu^{3+}$, J. Appl. Phys. **97**, 094312 (2005).

[54] A. K. Parchur and R. S. Ningthoujam, Behaviour of electric and magnetic dipole transitions of $Eu^{3+}$, $^5D_0 \rightarrow {}^7F_0$ and Eu–O charge transfer band in $Li^+$ co-doped YPO4:$Eu^{3+}$, RSC Adv. **2**, 10859 (2012).

[55] T. Kyshida, Linewidths and thermal shifts of spectral lines in neodymium-doped yttrium aluminum garnet and calcium fluorophosphate, Phys. Rev. **185**, 500 (1969).

[56] S. Saha, S. Prusty, S. Singh, R. Suryanarayanan, A. Revcolevschi, and A. K. Sood, Anomalous temperature dependence of phonons and photoluminescence bands in pyrochlore $Er_2Ti_2O_7$: Signatures of structural deformation at 130 K, J. Phys.: Condens. Matter **23**, 445402 (2011).

[57] M. G. Beghi, C. E. Bottani, and V. Russo, Debye temperature of erbium-doped yttrium aluminum garnet from luminescence and Brillouin scattering data, J. Appl. Phys. **87**, 1769 (2000).